Endocardial irrigated catheter for volumetric optoacoustic mapping of radio-frequency ablation lesion progression

Özsoy, Cagla ; Floryan, Marie ; Deán-Ben, Xose Luis ; Razansky, Daniel

DOI: https://doi.org/10.1364/OL.44.005808

Endocardial irrigated catheter for volumetric optoacoustic mapping of radio-frequency ablation lesion progression

Öszoy, Cagla ; Flroyan, Marie ; Deán-Ben, Xose Luis ; Razansky, Daniel

Optics Letters

Endocardial irrigated catheter for volumetric optoacoustic mapping of radio-frequency ablation lesion progression

ÇAĞLA ÖZSOY,[1,2] MARIE FLORYAN, [1,2] XOSÉ LUÍS DEÁN-BEN,[1,2] DANIEL RAZANSKY[1,2*]

[1]Faculty of Medicine and Institute of Pharmacology and Toxicology, University of Zurich, Switzerland
[2]Institute for Biomedical Engineering and Department of Information Technology and Electrical Engineering, ETH Zurich, Switzerland
*Corresponding author: daniel.razansky@uzh.ch

Received XX Month XXXX; revised XX Month, XXXX; accepted XX Month XXXX; posted XX Month XXXX (Doc. ID XXXXX); published XX Month XXXX

Radiofrequency (RF) catheter ablation is widely employed for various minimally invasive procedures, including treatment of tumors, cardiac arrhythmias and varicose veins. Accurate real-time monitoring of the ablation treatments remains challenging with the existing clinical imaging modalities due to the lack of spatial or temporal resolution or insufficient tissue contrast for differentiating thermal lesions. Optoacoustic (OA) imaging has been recently suggested for monitoring temperature field and lesion progression during RF interventions. However, strong light absorption by standard metallic catheters hindered practical implementations of this approach. Herein, we introduce a new RF ablation catheter concept for combined RF ablation and OA lesion monitoring. The catheter tip encapsulates a multimode fiber bundle for OA excitation with near-infrared light whereas the electric current is conducted through the irrigation solution, thus avoiding direct exposure of the metallic parts to the excitation light. We optimized the catheter diameter and the saline flow rate in order to attain uniform and deep lesions. The newly introduced hybrid catheter design was successfully tested by real-time monitoring of the ablation process in smooth ventricle and rough atrium walls of a blood-filled ex-vivo porcine heart, mimicking in vivo conditions in the clinical setting.

http://dx.doi.org/10.1364/OL.99.099999

Radiofrequency (RF) catheter ablation is routinely used in a myriad of clinical interventions such as cancer therapy [1], endovenous removal of varicose veins [2,3] or treatment of cardiac disorders [4]. The procedure is generally preferred over alternative thermal ablation approaches due to its low cost, minimal invasiveness and simplicity of operation [5]. Typically, RF ablation procedures are being performed under x-ray fluoroscopy guidance, which however offers poor soft tissue contrast, lacks three-dimensional (3D) information and carries certain risks due to the long exposure to x-rays [6]. Moreover, success rates of RF catheter ablation procedures critically depend upon the effective tissue impedance in the heat-affected area and the resulting spatio-temporal distribution of the temperature field. Development of non-invasive real-time monitoring methods is hence essential for optimizing outcomes of these treatments. To this end, several imaging modalities have been suggested for this purpose [7-11]. However, these are either limited by lack of contrast and sensitivity, the use of ionizing radiation, shallow penetration or insufficient spatio-temporal resolution [8,12].

Optoacoustic (OA) imaging has recently been proposed as a new approach for monitoring RF ablation procedures [13-17]. The method is based on tissue excitation with non-ionizing laser light and has shown considerable sensitivity to temperature changes and chemical transformations associated with tissue coagulation [14]. The temperature dependence of the OA signal intensity is associated to the Grüneisen parameter for temperatures below the coagulation threshold and becomes more complex at higher temperatures due to non-linear effects and additional changes of tissue optical properties [18]. Moreover, state-of-the-art systems are capable of real-time imaging in two and three dimensions with high spatial resolution [19], which was explored for monitoring of various thermal therapy interventions [14,20-21]. 3D imaging systems are known to be less prone to quantification errors and further enable mapping the entire volume of the induced lesion. In particular, feasibility of 3D mapping of temperature distribution and lesion progression during RF ablation has been demonstrated [15], albeit the excitation light was delivered through the imaging probe making it not practical for monitoring ablation treatments in deep human tissues like the atrial wall. We have recently introduced an integrated catheter design based on copper-coated fibers that enabled simultaneous delivery of the ablation current and near-infrared excitation light into the ablated region [16]. This forward-looking catheter enabled simultaneous delivery of the ablation current and the excitation laser light, yet significant image distortions were observed due to strong light absorption and acoustic reflections at the catheter tip.

In this work, we introduce a new catheter design concept where the ablation current is delivered via the irrigation saline solution,

thus averting direct exposure of any metallic parts to the excitation laser light (Fig. 1). The latter is provided via five multimode fibers encapsulated in the catheter tip. The step-index multimode fibers (Thorlabs, USA) have a core diameter of 600 µm and a numerical aperture (NA) of 0.50. The catheter is further composed of a T-type thermocouple and a metallic 23G x 3 1/8" needle (Sterican, B. Braun Melsungen AG, Germany) that functions as an ablation electrode and a passage for the saline irrigation [Fig. 1(b)]. The proximal end of the catheter features separate connectors to the RF signal generator, Maestro 3000, (Boston Scientific, Marlborough, U.S.) , data acquisition card, NI 9213 DAQ, for temperature recordings (National Instruments Corporation, Texas, U.S.)), syringe pump for continuous saline irrigation (World Precision Instruments, Sarasota, USA), and a tunable nanosecond laser source for the OA excitation (Innolas Laser GmbH, Krailling, Germany).

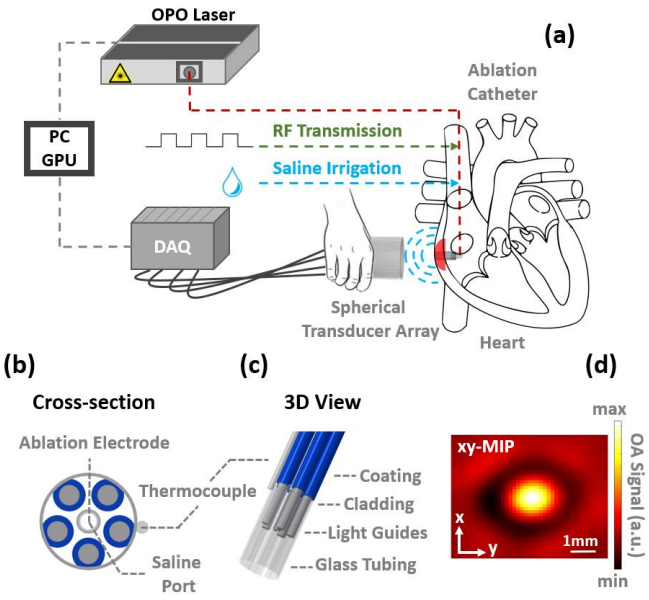

Fig. 1. Design and implementation of the RF ablation catheter. (a) Schematic representation of the OA approach for monitoring cardiac RF ablation. (b) Cross-sectional view of the integrated catheter tip comprising a fiber bundle, a thermocouple and an electrode. (c) 3D view of the proximal end of the catheter assembled within the tubing. (d) Top-view of the OA image of a microscope slide painted in black used to estimate the illumination pattern created by the fiber bundle.

The fibers were bundled within an optical fiber connector, stabilized using a high-temperature epoxy (353ND, Epoxy Technology, Inc. Billerica, MA) and polished to achieve optimal coupling to the outlet of the laser. At the distal end of the RF catheter, multimode fibers were cleaved to achieve maximum efficiency and arranged around the ablation electrode to fit within a 5 mm long (3 mm diameter) glass tubing (Bruker, Massachusetts, USA) [Figs. 1(b) and 1(c)]. Saline injection with a syringe pump (World Precision Instruments, Sarasota, USA) is canalized to the ablation electrode through a fine bore polythene tubing with 0.86 mm inner diameter (Smiths Medical Inc., Minnesota, USA). A high-density thermocouple module (National Instruments, Austin, USA) further enables temperature readings during RF ablation with a T-type thermocouple attached to the outer surface of the catheter [Fig. 1(b)]. The illumination pattern at the tissue surface was characterized by imaging a microscope slide painted in black with the OA system. The top-view of the 3D OA image is displayed in Fig.1(d). The measured pulse energy at the output of the fiber bundle was 2 mJ distributed over 8 mm^2 area on the tissue surface, which corresponds to a fluence of 25 mJ/cm^2 - within the ANSI safety standard at the 780 nm wavelength [22]. The light intensity is then expected to decay approximately one order of magnitude per centimeter within biological tissues at near infrared wavelengths [23].

OA monitoring of the RF ablation procedure was performed by collecting the signals generated in the illuminated tissue volume with a custom-made spherical matrix ultrasound detector array having 256 detection elements with central frequency of 4 MHz and 100% detection bandwidth, allowing for almost isotropic resolution of ~200 µm at the center of the sphere [24]. The ultrasound array was placed from the side of the heart opposite to the catheter [Fig. 1(a)] and filled with agar to ensure acoustic coupling between the heart tissue and detection elements. A custom-made data acquisition system (DAQ, Falkenstein Mikrosysteme GmbH, Taufkirchen, Germany) was used to digitize the generated OA signals at 40 mega-samples per second, being triggered by the Q-switch output of the OPO laser. The OA signals acquired during the RF ablation experiments were band-pass filtered with cut-off frequencies 0.1 and 3 MHz and processed with a model-based reconstruction algorithm to render 3D images of the ROI [25]. The reconstructed images were further corrected for the exponential light fluence decay in the axial direction.

The RF ablation efficiency of the endocardial irrigated catheter was evaluated by characterizing the lesions created with varying ablation parameters. Specifically, the coagulation depth was measured by manually segmenting the cross-sectional photographs taken after the procedure (Figs. 2a and 2b) as a function of the saline concentration, ablation duration, irrigation rate and the diameter of the catheter tip. RF ablation lesion characterization experiments were performed using freshly excised porcine heart tissues placed on top of a conductive grounding pad that served as ground electrode. The distal end of the RF ablation catheter (3mm tip diameter) was placed on the heart samples while its proximal end was connected to an RF generator delivering 20 kHz frequency electric signals with an average power of 10 W. Ablation lesion formation was accomplished by transmitting electrical current through different samples of heart tissue for 10, 30, 60, 90, 120, 240 and 300 seconds.

Same experiments were repeated by irrigating the 0.9% (physiological) and 3.6% (hypertonic) saline solutions which were prepared by pouring 9 and 36 g of sodium chloride (NaCl) respectively to one liter of distilled water and mixing it until the solution becomes transparent. The effect of the saline irrigation rate on lesion formation was evaluated for 1, 3, 6 and 9 ml/min irrigation rates using the syringe pump flow rate control. Figs. 2(a) and 2(b) display the lesion depth (mm) versus ablation time (s) for different saline solution concentrations (%) and irrigation rates (ml/min). The location of the endocardial catheter during the characterization experiments is indicated with a black arrow in Fig. 2(a-b). Clearly, deeper lesions are generated by higher saline concentrations. Overall, mean ablation depths attained for 0.9% saline concentration was 4 mm, while it increased to 5.5 mm for 3.6% saline concentration. The maximum lesion depth achieved with 0.9% saline concentration at 9 ml/min saline flow rate was 6 mm, while 9 mm lesions were generated with 3.6% saline concentration

at 6 ml/min saline flow rate. We observed that the lesion progressed gradually within the first 120 seconds while no significant changes were noticed between 120 and 240 seconds. The saline concentration and the flow rate affect the electrical conductivity and hence are expected to have an effect on the formed lesion. High saline irrigation rates have an additional cooling effect that prevents excessive heating and decreases the possibility of tissue charring. The influence of these effects is however difficult to quantify, and we did not observe a clear dependence of the lesion depth upon the flow rate of the saline solution.

In a different set of experiments, dependence of the lesion depth upon the catheter tip diameter has been examined. Here we kept the saline concentration and the irrigation rate at 0.9% and 9 ml/min, respectively, and RF ablation was maintained for 300 seconds. As expected, the observed lesion depths increase from 3.5mm to 6.5 mm when increasing the catheter diameter from 2mm to 4mm. Note, however, that clinical RF ablation catheters normally measure 5-8 French (1.66-2.66 mm) to prevent vessel damage during the catheterization procedure. Since the 2 mm catheter was only capable of creating superficial lesions, the 3 mm catheter tip was selected for the final design due to its consistent ablation performance and relatively small size.

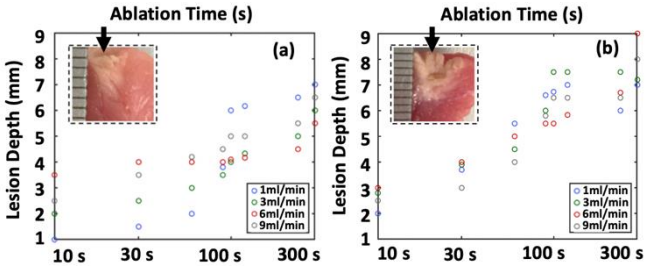

Fig. 2. Dependence of the lesion depth (mm) upon ablation time. (a) Lesions formed by 0.9% saline solution with different saline irrigation rates. (b) The corresponding lesions formed by 3.6% saline solution. The photographs from sliced specimen show representative examples of the ablation lesions formed by irrigating saline with 6 ml/min for 30 s (a) and with 9 ml/min irrigation rate for 240 s (b).

In the first OA monitoring experiment, we evaluated the feasibility to image a tissue sample under realistic in vivo imaging scenario with the highly absorbing blood background. We therefore mimicked a typical cardiac or endovenous procedure by inserting the RF catheter in a plastic chamber filled with fresh porcine blood, which is meant to be removed by irrigating the saline solution. OA imaging at 780 nm (isosbestic point of hemoglobin) was then performed during irrigation of the saline. In the resulting images, the bright OA signal in the beginning of the procedure [Fig. 3(a)] originates from blood in contact with the tip of the fiber bundle (pre-irrigation). As the irrigation progresses, the blood is slowly removed from the catheter tip with a mixture of blood and saline remaining in the cavity so that more light can propagate toward the catheter edge. As a result, both tips of the fiber bundle and the catheter turn visible [Fig. (3b)]. The gradual saline irrigation effects can be best perceived in Visualization 1 showing real-time evolution of the OA images. The images mainly feature the edges between regions with different blood concentration, which is ascribed to the limited angular coverage of the transducer array and the associated limited-view image artifacts [26]. At a later stage (post-irrigation), all the blood is removed from the catheter tip, making it transparent for the light delivery. This results in bright signals from the blood interface surrounding the catheter tip [Fig. (3c)], each step during perfusion of saline are further schematically represented in Fig. 3(d-f). The experimental arrangement of the OA imaging system relative to the endocardial catheter, placed in direct contact with the blood-filled sample chamber, is shown in Fig. 3(g). The field of view in panels a-c corresponds to the blood volume represented in Fig. 3(g).

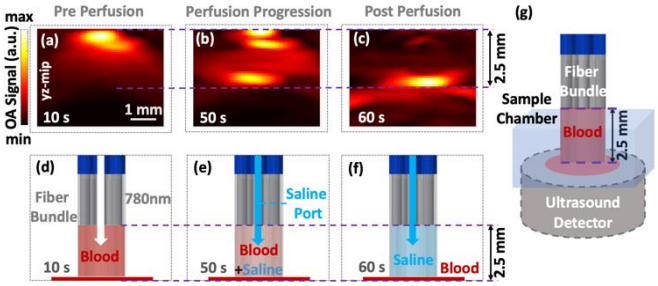

Fig. 3. Real-time OA imaging of saline irrigation in the course of blood removal from the catheter cavity. (a) OA image acquired before the saline irrigation starts, when the catheter is filled with the porcine blood. (b) The corresponding image acquired during the saline irrigation process. (c) The image acquired immediately after the catheter cavity was fully perfused with saline. (d-f) Schematic lay-outs of the experimental arrangement in relation to the reconstructed OA images. (g) Experimental arrangement of the OA imaging system relative to the endocardial catheter.

In the second experiment, real-time OA monitoring of RF ablation progression was performed in an ex-vivo porcine heart filled with blood to mimic typical conditions in a clinical setting. Both the heart ventricle and atrium were ablated by employing the same RF generator parameters as described in the characterization experiments. Throughout the ablation procedure, 3.6% saline solution was irrigated at 1 ml/min rate. The laser wavelength was set to 780 nm corresponding to the maximum OA contrast achieved between coagulated and non-coagulated tissues [15]. OA signals were then acquired for 200 s, including 20 seconds before the RF generator was activated, 100 seconds during the ablation procedure and 80 seconds during the cool-down phase. It was observed that larger and deeper lesions were produced on the smooth ventricular wall while electric contact was presumably compromised by the rough atrial surface. A clear increase of the OA signal in the ex-vivo porcine ventricle tissue was perceived in the entire ROI while the signal intensity was lowest prior to the activation of the RF energy [Fig. 4(a-c)]. This is partially attributed to the changes in the Grüneisen parameter caused by temperature increase due to resistive heating of the heart muscle [14]. The OA signal is additionally altered by tissue coagulation [27]. Overall, the ablated region in the sliced specimen [Fig. 4(d)] corresponds well to the shape of the yellow-colored area exhibiting elevated OA signal in the post-ablation OA image in Fig. 4(c). The temporal evolution of the OA readings in two representative voxels is further shown in Fig. 4(e). The OA signal at the end of the acquisition is higher than in the pre-ablation region, due to continuing cooldown. Also, the signal in the coagulated area [purple square in Fig. 4(c)] did not decrease significantly during the cool-down phase [purple plot in Fig. 4(e)]; this could be mainly attributed to an increase in optical absorption coefficient caused by the denaturized proteins in this region [18].

In this work we devised a new approach for real-time OA monitoring of thermal lesion formation during RF ablation

treatments. Owing to the indirect transmission of the RF current into the tissue through the irrigation saline solution, image artefacts associated with light absorption by metallic components or acoustic reflections at the catheter tip can be avoided. Active cooling provided by irrigated catheters is in fact an established method implemented in clinical cardiac RF ablation procedures that has been shown to increase efficiency of the lesion generation and reduce the risk of tissue charring and steam pops [28]. In the ex-vivo porcine heart ablation experiments different chambers of the heart were successfully ablated providing uniform coagulum without any tissue charring, while the OA signal variations associated with the temperature increase and chemical transformations during coagulation could be monitored in real-time. In general, the lesions developed in the atrium were shallower than those developed in the ventricle. This can be attributed to the more heterogeneous structure of the atrium wall and the compositional differences between two chambers. However, the fact that coagulation could still be produced under this challenging scenario indicates the general usability of the catheter for real clinical application. Design optimizations may still result in a better performance on rough surfaces. Also important is the fact that relatively deep ablation lesions could be produced in calibration experiments for a relatively small catheter diameter as well as low saline concentrations and irrigation rates. Minimal irrigation rates were dispensed in all ablation experiments. In this way, potential damages, such as pulmonary edema or pleural effusion, can be avoided, even when using hypertonic saline concentrations. The lesion depths achieved in most our experiments may however not suffice for some cardiac RF ablation procedures so that larger catheter diameters are deemed necessary. The reason for shallow ablation lesions can be explained by tissue heterogeneities, which lead to sub-optimal catheter-tissue contact and the need to apply force to guarantee good coupling. Certain degree of pressure is required for controlled ablation, which is crucial for averting damage to the neighboring healthy tissue and the risk of cardiac tamponade [29]. The endocardial catheter may also be a useful tool in anticoagulation therapy [30]. The ablation performance can also be enhanced by incorporating mechanical force feedback from the catheter tip in future catheter designs as different risk levels of cardiac perforation are imposed by atria and ventricles due to their different wall thickness [31].

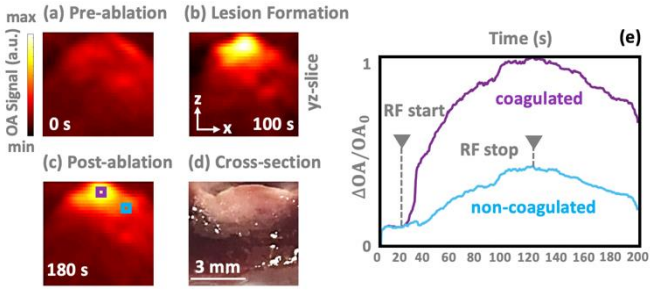

Fig. 4. Real-time OA monitoring of RF ablation in ex-vivo porcine heart. Lateral views of fluence-corrected OA images acquired from the ventricle at different time points during the treatment; before ablation started (a), during the lesion formation (b) and the cool-down period (c). Post-ablation photograph of a sliced ventricular specimen showing the generated RF ablation lesion (d). Time course of the relative change of OA signal (ΔOA/OA) in a coagulated (purple) versus non-coagulated (blue) voxels, as labelled in panel (e).

Supplementary material.
(1) The gradual saline irrigation effects within the catheter visualized by the real-time evolution of the OA images.

Funding. German Research Foundation (DFG) (RA 1848/5-1).

Disclosures. The authors declare no conflicts of interest.

References

1. E. Buscarini, A. Savoia, G. Brambilla, F. Menozzi, L. Reduzzi, D. Strobel, J. Hänsler, L. Buscarini, L. Gaiti, A. Zambelli, ER **15**, 884 (2005).
2. A. Kayssi, M. Pope, I. Vucemilo, C. Werneck, Can J Surg. **58**, 85 (2015).
3. T. F. Fehm, X. L. Deán-Ben, P. Schaur, R. Sroka, D. Razansky, J. Biophotonics **9**, 934 (2016).
4. J. P. Joseph, K. Rajappan, Q. J. Med. **105**, 303 (2011).
5. M. Ahmed, C. Brace, F. T. Lee, S. N. Goldberg, Radiology **258**, 351 (2011).
6. C. Gianni, A. Natale, Heart Rhythm **14**, 817 (2017).
7. C. Eitel, G. Hindricks, M. Grothoff, M. Gutberlet, P. Sommer, Curr. Cardiol. Rep. **16**, 511 (2014).
8. C. P. Fleming, K. J. Quan, H. Wang, A. M. Rollins, Opt.Express **18**, 3079 (2010).
9. S. G. Demos, S. Sharareh, Opt. Express **16**, 15286 (2008).
10. M. Granier, P. F. Winum, M. Granier, P. Liaud, G. Cayla, P. Messner, J. L. Pasquie, I. Schuster, Heart Rhythm **12**, 1827 (2015).
11. A. Niko Zadeh, Ö. Oralkan, M. Gencel, J. W. Choe, D. N. Stephens, A. de la Rama, P. Chen, F. Lin, A. Dentinger, D. Wildes, K. Thomenius, K. Shivkumar, A. Mahajan, C. H. Seo, M. O'Donnell, U. Truong, D. J. Sahn, P. T. Khuri-Yakub, in Proc. IEEE Ultrason. Symp. (2010).
12. R. Ranjan, E. G. Kholmovski, J. Blauer, S. Vijayakumar, N. A. Volland, M. E. Salama, D. L. Parker, R. MacLeod, N. F. Marrouche, Circ. Arrhythm. Electrophysiol. **5**, 1130 (2012).
13. Dana, L. Di Biase, A. Natale, S. Emelianov, R. Bouchard, Heart Rhythm **11**, 150 (2014).
14. I. V Larina, K. V. Larin, R. O. Esenaliev, J. Phys. D: Appl. Phys. **38**, 2633 (2005).
15. G. A. Pang, E. Bay, X. L. Deán-Ben, D. Razansky, J.Cardiovasc. Electrophysiol. **26**, 339 (2015).
16. J. Rebling, F. J. Oyaga Landa, X. L. Deán-Ben, A. Douplik, D. Razansky, Opt. Letters **43**, 1886 (2018).
17. S. Iskander-Rizk, P. Kruizinga, A. F. W. van der Steen, G. van Soest, Biomed. Opt. Express **9**, 1309 (2018).
18. F. J. Oyaga Landa, X. L. Deán-Ben, R. S., D. Razansky, Sci. Rep.**7**, 9695 (2017).
19. E. Merčep, J. L. Herraiz, X. L. Deán-Ben, D. Razansky, Light: Science & Applications **8**, 1 (2019).
20. V. A. Serebryakov, É. V. Boĭko, A. V. Yan, J. Opt. Technol. **81**, 312 (2014).
21. S. H. Wang, C. W. Wei, S. H. Jee, P. C Li, in Proc. SPIE (2009).
22. American National Standards Institute LIoA. American National Standard for the Safe Use of Lasers ANSI Z136.1-2000. American National Standards Institute, Inc; New York: 2000.
23. S. L. Jacques, Phys. Med. Biol. 58, R37-61 (2013).
24. X. L. Deán-Ben, D. Razansky, Opt. Express **21**, 28062 (2013).
25. L. Ding, X. L. Deán-Ben, D. Razansky, IEEE T-MI, **9**, 1858 (2017).
26. X. L. Deán-Ben, H. López-Schier, D. Razansky, Sci. Rep. **7**, 6850 (2017).
27. K. V. Larin, I. V. Larina, R. O. Esenaliev, J. Phys.D:Appl.Phys. **38**, 2645 (2005).
28. A. Müssigbrodt, M. Grothoff, B. Dinov, J. Kosiuk, S. Richter, P. Sommer, O. A. Breithardt, S. Rolf, A. Bollmann, A. Arya, G. Hindricks, Biomed. Res. Int. **2015**, 389294 (2015).
29. R. Hamaya, S. Miyazaki, H. Taniguchi, S. Kusa, H. Nakamura, H. Hachiya, T. Kajiyama, T. Watanabe, M. Igarashi, K. Hirao, Y. Iesaka, EP, **20**, 1776 (2018).
30. A. S. Jeevarathinam, N. P. Kevin, H. A. Hariri, J. Wang, Y. Bai, L. Wang, T. Hancock, S. Keys, W. Penny, J. V. Jokerst, Biosensors and Bioelectronics 126, 831-837 (2019).
31. M. Tokuda, P. Kojodjojo, L. M. Epstein, B. A. Koplan, G. F. Michaud, U. B. Tedrow, W. G. Stevenson, R. M. John, Circ. Arrhythm Electrophysiol. **4**, 660 (2011).